

Supplementary Materials for Computational Discovery of Microstructure Families

Desai Chen, Mélina Skouras, Bo Zhu, Wojciech Matusik.

correspondence to: desaic@csail.mit.edu

This file includes:

Supplementary Text
Figs. S1 to S7
Tables S1, S2
Captions for Movies S1 to S3

Other Supplementary Materials for this manuscript includes the following:

Movies S1 to S3
Microstructure gamut and templates

Supplementary Text

Cubic Symmetry

All our structures are cubic symmetric by construction. This is enforced by defining structures inside a single control tetrahedron and mirroring it to 48 copies. To be more precise, we first define our structures to be in the interval $[0,1]^3$. The material assignment at each point in the interval is controlled by a reference point in the control tetrahedron. First, a point (x_1, x_2, x_3) outside the interval $[0,0.5]^3$ is mapped to a point (x_1', x_2', x_3') inside the interval by the relationship $x_i' = 1 - x_i$ to enforce orthotropic symmetry. Then, a point (x_1, x_2, x_3) inside the interval $[0,0.5]^3$ is mapped to a new point (x_1', x_2', x_3') such that the new coordinates are a permutation of the original coordinates and $x_1' \geq x_2' \geq x_3'$. Geometric symmetry guarantees that all structures have elastic tensors with only 3 free parameters: Young's modulus E , Poisson's ratio ν and shear modulus G . The symmetric stress-strain tensor C expressed using these free parameters is

$$C = \frac{E}{(1+\nu)(1-2\nu)} \begin{pmatrix} 1-\nu & \nu & \nu & 0 & 0 & 0 \\ \nu & 1-\nu & \nu & 0 & 0 & 0 \\ \nu & \nu & 1-\nu & 0 & 0 & 0 \\ 0 & 0 & 0 & G & 0 & 0 \\ 0 & 0 & 0 & 0 & G & 0 \\ 0 & 0 & 0 & 0 & 0 & G \end{pmatrix}.$$

For each structure, only two simulations (a stretching and a shearing deformation) are needed to determine the three parameters. This is much simpler than the generic case, as an orthotropic structure requires 6 simulations to compute all necessary elasticity parameters.

Gamut Representation and Exploration

The material gamut is represented and explored using the methods outlined in (26). We use a signed-distance function $\Psi(x)$ defined on a background grid to represent the range of achieved material properties. The boundary of the gamut is the set of points satisfying $\Psi(x)=0$ while the interior is defined to be the set corresponding to $\Psi(x)<0$. The gamut exploration iterates between a discrete sampling stage and a continuous optimization stage. For both steps, a random subset of structures are chosen as seeds for expansion. Points near the current gamut boundary are preferred since they often have distinctive topologies. For each point, a target point in the material space is defined along the signed-distance gradient direction to expand the gamut. In the discrete sampling stage, a seed structure is randomly altered by adding or removing beams. In our current implementation of the discrete sampling step, candidate structures are generated purely based on geometry. To maintain the connectivity of the structures for single-material printing, disconnected components are removed and enclosed holes are filled before the structures are added to the database. It is possible to incorporate more information such as stress analysis of the seed microstructure into the discrete sampling step. The continuous optimization is similar to previous work (24) with modified objective functions and constraints. Specifically, we do not need to enforce any cubic symmetry constraint in the elasticity tensor since it is satisfied by construction. We do not have equality constraints for the shear modulus or the volume ratio either since our primary

goal is to explore the gamut of material properties rather than to find specific structure designs. The objective function to minimize is the squared distance to the target macroscopic material properties. Each quadratic objective term is weighted automatically to have the same value range between 0 and 1. To avoid overly complex structures and thin features, we use sensitivity smoothing with a radius of 3 voxels to limit the smallest feature size to 2 voxels. The minimization problem is solved using the method of moving asymptotes (40). Each optimization is set to run for at most 50 steps. We then convert the optimized continuous distributions to discrete distribution by thresholding. The threshold values step from 0.1 to 0.5 at an interval of 0.1. All thresholded discrete structures are automatically cleaned up and added to the gamut.

Template Extraction and Fitting

We have chosen to use a set of cuboids to represent a template. We provide the five auxetic templates reported in this work as a function that computes a discretized structure at specified resolutions given two reduced parameters (30). The set of beams can be voxelized and smoothed at arbitrary resolutions to generate new discrete structures. To fit the set of beams to a given structure, we use gradient descent with numerical differentiation to compute the gradients. We use Euclidean norm as the distance metric to measure the per-voxel material difference between a target structure and the generated structure. To avoid discontinuities in the objective function, we convert the material distribution of both structures to continuous variables and apply a smoothing filter. The filter has a radius of 4 voxels with linearly decaying weights. Since the objective function used for the template fitting is highly non-convex, we need a good initial guess for the number of beams and their initial arrangement. We use the morphological skeleton (29) of the target structure to help us find the initial beam configuration. The skeletonization step converts a 3D binary material assignment to a small subset of voxels that represents the skeleton of the structure (Fig. S3B). From the skeleton, we construct a graph by connecting neighboring voxels. The graph is then simplified by collapsing paths into single edges (Fig. S3C). A path is a sequence of connected vertices where all intermediate vertices have valence 2. We then iteratively add back the furthest vertices to the simplified path until no vertex in the original graph deviates away by more than a threshold of 0.02. The simplified graph is converted to a template by placing cuboid beams on each edge (Fig. S3D). To smooth the connections between the beams, we place dome-shaped caps at the endpoints of each beam. The cross-section sizing and orientation of each cuboid are initialized individually to minimize the Euclidean norm between the cuboid and the smoothed input structure. We then run gradient descent with central differencing to adjust all cuboid parameters including cuboid endpoint positions to arrive at a final fitted structure (Fig. S3E). In the gradient descent step the connectivity constraint between edges is relaxed to allow a vertex to be connected to the middle of another edge.

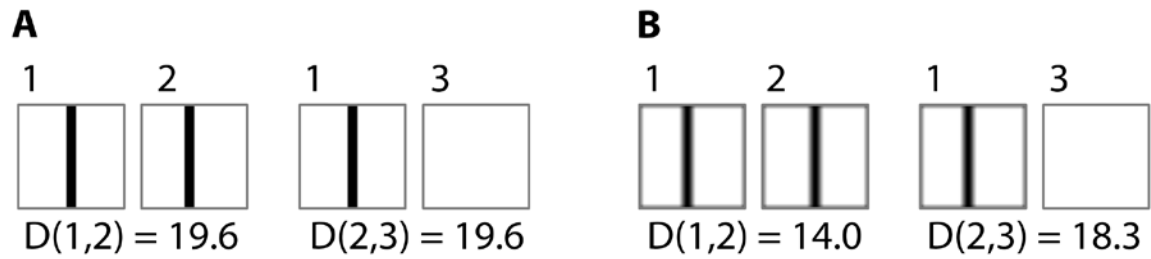


Fig. S1

Smoothing for geometric difference metric. (A) Euclidean norm measured on exemplar 2D structures at 64^2 resolution. Structures 1 and 2 contain a single vertical beam shifted by 3 voxels. Structure 3 is an empty structure. The Euclidean norm between structure 1 and 2 is the same as the distance between 1 and 3. Nonlinear dimensionality reduction methods based on distance matrices will treat the three structures as equally different from each other. However, structure 1 and 2 are much more similar in terms of shape and physical properties. (B) After applying a smoothing filter on the structures, the difference between 1 and 2 is significantly lower than 1 and 3. 3 can be separated more easily.

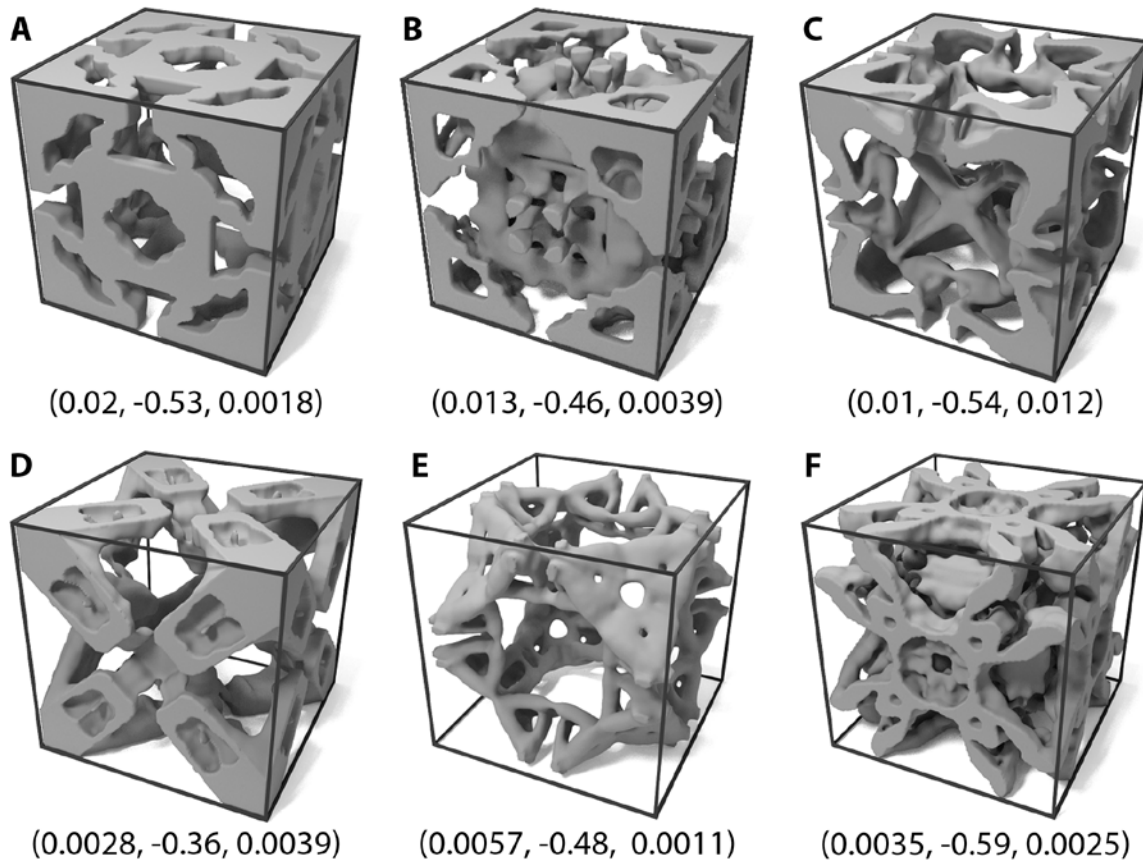


Fig. S2

Examples of auxetic structures in addition to the five selected families in the main paper. Each structure is labeled by its relative Young's modulus, Poisson's ratio and relative shear modulus. **(A)** A 3D structure constructed by repeating on each cube face a 2D cubic structure. Such 3D structures have low shear modulus due to the lack of internal structures that resist diagonal compression. The example structure has a low shear modulus ratio of 0.09. **(B)** A structure similar to **(A)** with more resistance to shear deformation. The rectangular components in **(A)** is replaced by a cubic core around the center of the structure. **(C)** A structure similar to those in Family 5 with good resistance to shearing. However, this structure has an overly complex core. **(D)** This structure is similar to those in Family 3 without the central core. The structure is relatively simple and has good shear resistance. However, this structure contains very thin connections that are not suitable for current fabrication technology as manifested by its low relative Young's modulus. This example shows that there are more simple geometries worth exploring for future work. **(E)** This structure is similar to those in Family 4 without the core piece. It has a much lower shear resistance than the structures of Family 4. **(F)** An overly complex structure with intricate features obtained by topology optimization without filtering. Such structures are difficult to manufacture and thus are not selected for analysis.

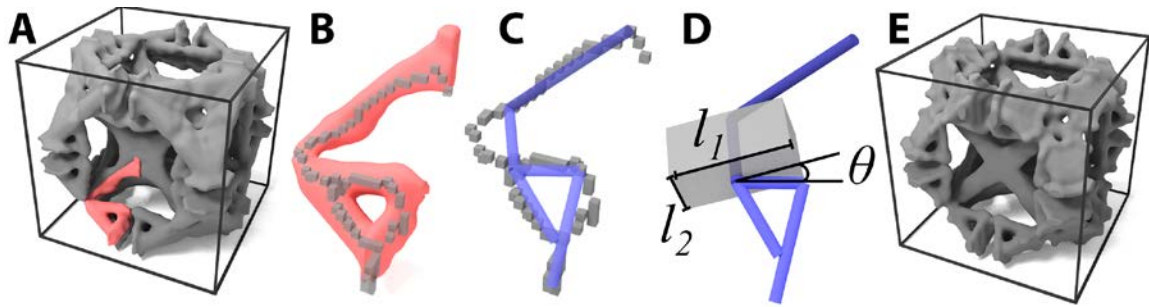


Fig. S3

Computing a microstructure template from a representative structure. For an input structure (**A**), we only need to analyze one tetrahedral slice (highlighted in red) of the whole structure due to its cubic symmetric construction. A morphological skeleton is extracted from the portion of the structure (**B**). The skeleton is a sequence of voxels. They are converted into a graph by connecting neighboring voxels. The graph is simplified (**C**) by merging paths into single edges while maintaining an error threshold. A cuboid (**D**) is placed on each edge of the simplified graph. The figure shows an example of a cuboid that lines up with the endpoints of its edge. In addition to coordinates of its endpoints, the cuboid is parameterized by side lengths (l_1 , l_2) of the cross section and a tilting angle θ . (**E**) The final structure generated by the template using fitted parameters is shown. Its geometry closely resembles the input structure while its component are noticeably less curved.

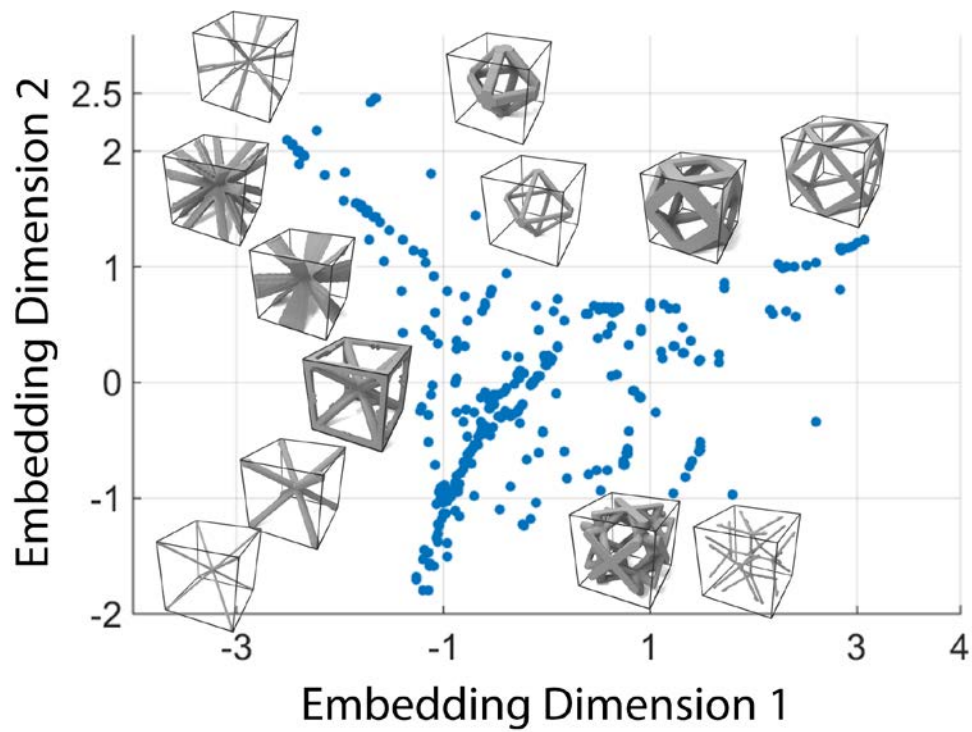


Fig. S4

Structures with large Poisson's ratios ($\nu > 0.3$). The embedding is computed using Isomap with 3 dimensions while the plot shows the 2D projection of the embedding. Structures with a positive Poisson's ratio have relatively simple topologies. Most structures are controlled by a single beam reflected according to cubic symmetry.

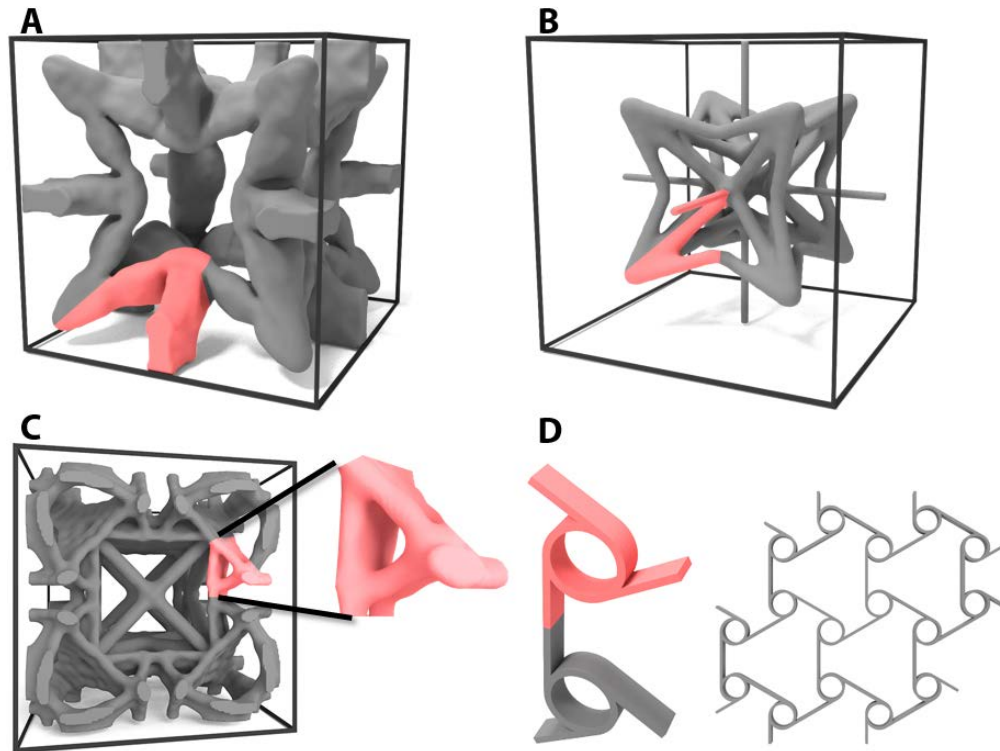


Fig. S5

Microstructures that resemble designs from previous works. (A) A reentrant structure in our database similar to the conceptual sketch (B) proposed by Lakes (18). Both structures have very low shear modulus ratio (0.05-0.15). Our structure is simpler with only two control beams reflected by cubic symmetry while (B) has three beams (highlighted in red). (C) The rotating triangle mechanisms resembles 2D chiral structures (19). (D) An anti-trichiral lattice (36) has unit nodes most similar to our rotating triangle joints highlighted in red.

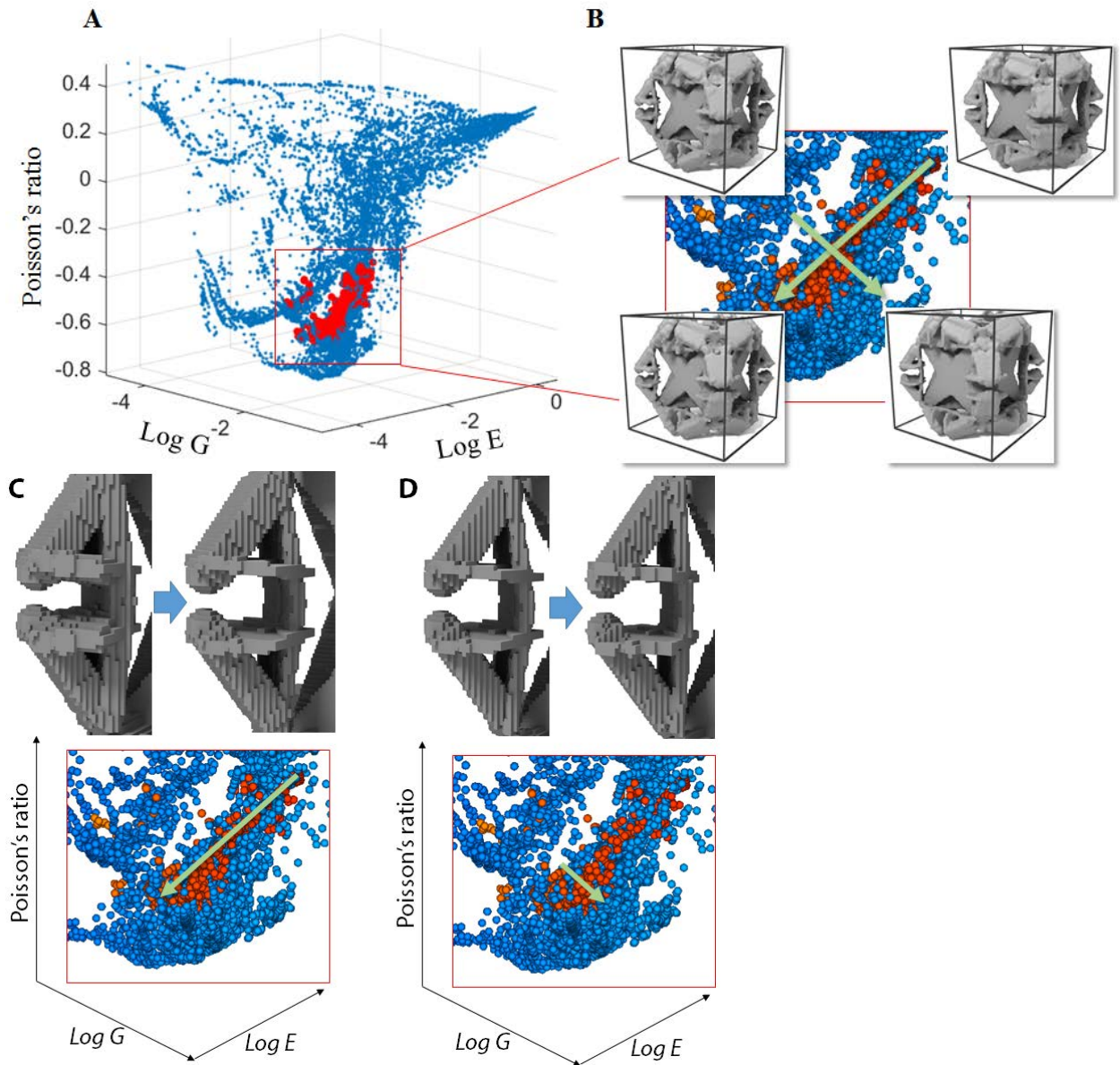


Fig. S6

Reduced parameters for Family 4. The distribution of the parameters corresponding to Family 4 is shown as red points in (A). The two principal directions are shown as green arrows in (B). The first direction reduces the Young's modulus and Poisson's ratio by decreasing the joint thickness (C). The second direction increases the shear modulus by slightly rotating the triangle joints outward (D). An animation of the shape changes is shown in movie S2.

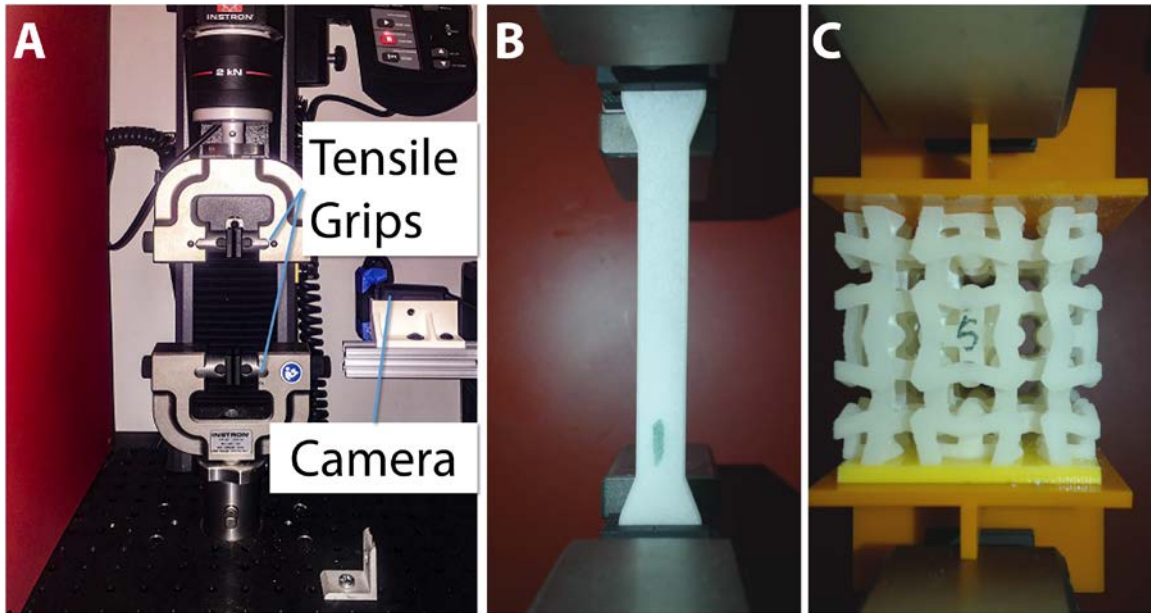


Fig. S7

Test apparatus for measuring Young's modulus and Poisson's ratio. (A) Instron 5944 for mechanical testing. (B) Tensile test of printing materials. (C) Compression test of microstructures. The Poisson's ratio is calculated using vertical displacements and horizontal displacements. The vertical displacement is read from both the tensile test machine and the camera for redundancy. The horizontal displacement is measured using the camera only.

Table S1

Auxetic families and templates. *Column 2:* cluster sizes for the five families found by the family identification step. *Column 3:* skeletons of the templates. Each template is obtained from mirroring a small number of control beams (*Column 4*) according to cubic symmetry. *Column 5:* number of parameters and control beams in each template. Each control beam has 9 parameters--6 for positions of its endpoints and 3 for the cross section size and orientation. *Column 6:* Number of reduced parameter directions for each family. Directions that change the material properties by more than 10% are stored for tuning the structures. *Column 7:* Range of shear modulus ratio is computed among structures with Poisson's ratio -0.6 ± 0.05 .

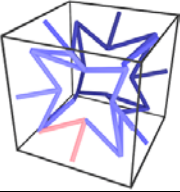
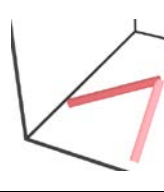
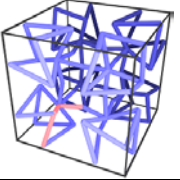

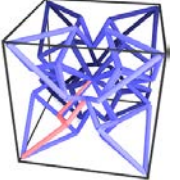
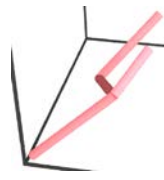
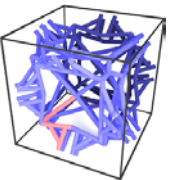

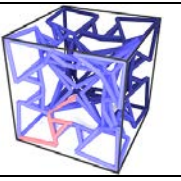


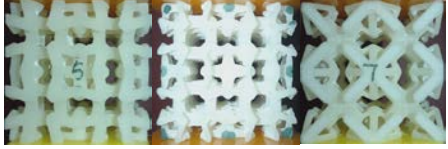

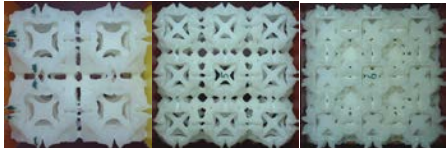

#	Sample size	Template Skeleton	Control Beams	Template parameters	Reduced	Range of G'
1	424			18 (2 beams)	2	0.07-0.14
2	367			27 (3 beams)	2	0.09-0.34
3	751			36 (4 beams)	2	0.34-0.90
4	881			45 (5 beams)	2	0.52-1.19
5	878			54 (6 beams)	2	0.5-1.02

Table S2

Simulated and measured Poisson's ratios of example structures. *Column 2:* homogenized Poisson's ratio; *Column 3:* Poisson's ratio simulated with a Neo-Hookean material model at 7% compressive strain; *Column 4:* measured Poisson's ratio of the printed structure at 7% strain. Due to fabrication variations including geometric thickening, printing orientation and incomplete support removal, we observe noticeable variance across the different measurements of the Poisson's ratios. Measurement errors due to camera misalignment and incorrect block placement cause additional variations (± 0.03) when we measure the same block multiple times. The linear material model is inaccurate in predicting the Poisson's ratios under our loading conditions at 7% strain while the non-linear material model (Neo-Hookean) is more accurate. For example, for Family 1, the linear material model predicts a lower Poisson's ratio than the measurement since the Poisson's ratio decreases as the strain increases. For Family 2, the trend is the opposite of that of Family 1 and the Poisson's ratio increases as the load increases.

Family	Linear simulation	Neo-Hookean	Measured Poisson's ratio
1 	-0.58	-0.71	-0.78 ± 0.03
	-0.62	-0.71	-0.68 ± 0.04
	-0.64	-0.70	-0.68 ± 0.04
2 	-0.68	-0.61	-0.61 ± 0.06
	-0.65	-0.57	-0.55 ± 0.10
	-0.73	-0.58	-0.58 ± 0.14
3 	-0.63	-0.49	-0.49 ± 0.03
	-0.64	-0.48	-0.47 ± 0.03
	-0.62	-0.48	-0.45 ± 0.04
4 	-0.62	-0.62	-0.62 ± 0.05
	-0.69	-0.67	-0.69 ± 0.13
	-0.52	-0.50	-0.45 ± 0.03
5 	-0.51	-0.51	-0.62 ± 0.07
	-0.68	-0.68	-0.58 ± 0.04
	-0.61	-0.61	-0.52 ± 0.03

Movie S1

Continuous search of a microstructure using topology optimization. The initial structure is a simple cubic frame with Poisson's ratio = 0.03 and a relatively low shear modulus. The target material parameters of this example is to decrease Poisson's ratio to -0.6 while increasing shear modulus. The optimized structure is a continuous distribution of materials where white means higher material density and black is lower density. The structure is thresholded at density = 0.5 to obtain a final discrete structure with Poisson's ratio = -0.6 and nearly isotropic shear modulus.

Movie S2

Shape variation of structures from Family 4 along principal directions. Since the shape variations (Fig. S6) are subtle especially along the second principal direction, we animate the gradual change of shape along the two principal directions. The first principal direction decreases the thickness of the rotating triangle joint while the second direction move the joint outwards.

Movie S3

Compression testing and simulation of example from Families 1, 3, and 5. For each structure, we show a measurement footage played back at 20x speed and a closeup of simulation with nonlinear material model (Neo-Hookean). The deformation qualitatively matches the footage where the most significant deformations occurs at the joint locations. We also provide an overlay of simulation and measurement footages to show the high degree of simulation accuracy.